SUPPLEMENTARY DATA FOR:

A Baltic heritage in Scotland: basement terrane transfer during the Grenvillian orogeny

1. Rock descriptions

Loch Fada inlier: intermediate orthogneiss *(sample RS-MTZ-18-01; UK National Grid Reference NC 4388 5509)*

The Loch Fada inlier was sampled c. 10 m above the Moine Thrust and hence is highly deformed. It is characterised by an intense, mm-scale mylonitic banding resulting in alternation of micaceous and felsic layers. Occasional pink granitic layers a few cm thick may represent mylonitised granitic veins. In thin section, the sample is strongly-foliated comprising alternating mafic and felsic bands up to a few millimetres in thickness. The mafic bands mostly comprise fine-grained (<0.5 mm) chlorite and epidote, with minor quartz, plagioclase and biotite. The felsic bands are dominated by porphyroclasts of inclusion-rich plagioclase up to 3 mm across and mosaics of recrystallised quartz, with subordinate chlorite, white mica and epidote. Accessory minerals include titanite and zircon.

Achininver inlier: felsic orthogneiss *(RS-TI-18-05; NC 5725 6477)*

A sample of felsic orthogneiss was obtained from immediately below the contact with structurally overlying Moine metasedimentary rocks. It is fine- to medium-grained and characterised by a compositional banding developed on a scale of 1–5 cm as a result of variations in the relative proportions of quartz, plagioclase, K-feldspar and white mica. In thin section, the sample is a felsic schist, dominated by quartz (<0.5 mm), muscovite (up to 1 mm long) and epidote (<0.3 mm) with minor feldspar. Muscovite defines a strong foliation, within which quartz shows a shape-preferred orientation. Accessory minerals include (in abundance order) apatite, titanite, zircon and rutile.

Achininver inlier: intermediate orthogneiss *(RS-TI-18-10; NC 5807 6410)*

The sample was obtained from the central part of the inlier. It is medium-grained and characterised by a 2–3 cm wide compositional banding that reflects variations in the relative proportions of biotite, hornblende, plagioclase feldspar and quartz. In thin section, texturally early, aligned hornblende laths are variably replaced by grains and elongate aggregates of biotite. Layers dominated by biotite and hornblende alternate with felsic layers largely composed of plagioclase with minor quartz. Accessory minerals include (in abundance order) pyrite, apatite, titanite, and zircon.

Felsic clast in Moine basal conglomerate *(RS-TI-18-07; NC 5740 6477)*

A clast of felsic composition was sampled from the Strathan metaconglomerate (Holdsworth et al. 2001) ~2–3 m above the contact with the Achininver inlier on the south side of Achininver Bay. The clast measured c. 30 cm in its longest dimension and was c. 2 cm thick.

Felsic clast in Moine basal conglomerate *(RS-TI-18-09; NC 5725 6500)*

A clast of felsic composition was sampled from the Strathan metaconglomerate ~1 m above the contact with the Achininver inlier on the north side of Achininver Bay. The clast measured ~50 cm in its longest dimension and was ~2 cm thick.

In hand specimen, both samples were fine-grained quartz-muscovite-feldspar schists. In thin section, both clasts comprised mainly (>90%) serrated quartz grains up to 1 mm across with minor fabric-forming muscovite and feldspar. Thin bands of fine-grained quartz are oriented parallel to the foliation and record strong grain-size reduction. Accessory minerals include apatite, zircon and rare rutile. The heavy fraction of RS-TI-18-07 contains (in abundance order) apatite, zircon, rutile, and monazite. The heavy fraction of RS-TI-18-09 contains (in abundance order) zircon, apatite, and xenotime.

Loch Shin inlier: mafic orthogneiss *(RS-LSI-18-21; NC 5207 1470)*

The sample is a hornblende-garnet-biotite gneiss which is characterised by a coarsely-developed cm-scale banding defined by 1-10 mm scale quartzofeldspathic layers and streaks that are inferred to be the result of high-grade metamorphism (Fig 3d). In thin section, a crude foliation is defined by irregular, ragged grains and aggregates of hornblende up to 2-3 mm size that are variably replaced by biotite and epidote. Plagioclase grains and aggregates up to 5 mm size are strongly sericitised and wrapped by mm-scale bands of recrystallized quartz that are oriented parallel to the hornblende-rich layers. Accessory phases include (in abundance order) pyrite, apatite, zircon, titanite, and chalcopyrite.

Loch Shin inlier: felsic sheet *(RS-LSI-18-20; NC 5190 1385)*

Deformed felsic pegmatites are locally common within the orthogneisses of the inlier. They are strongly deformed and/or lineated but in some cases it is still possible to demonstrate an original intrusive origin as their margins cut at a low angle across the gneissic banding in the host. The sample was obtained from a prominent 2 m thick intrusive sheet. In thin section, the sample comprises subhedral to anhedral K-feldspar, quartz and plagioclase, up to 1 mm across, along with rare ragged grains of muscovite. The feldspars are variably altered in their cores and along grain boundaries. Several grains, in particular of quartz, show a shaped-preferred orientation that defines the foliation. Thin, discontinuous veins up to 1 mm wide are dominated by quartz (>90%) and oriented subparallel to the foliation. Accessory minerals include (in abundance order) zircon, apatite, pyrite, rutile, xenotime, and uraninite.

Loch Shin inlier: biotite schist *(RS-LSI-18-19; NC 5208 1388)*

A thin strip of marble and biotite schist, no more than a few tens of metres thick, occupies the centre of the inlier (Read & Phemister 1926). The sample is a fine-grained, brown-weathering biotite schist. In thin section, the sample is a schist dominated by biotite, plagioclase, quartz, perthitic K-feldspar and Fe–Ti oxides and sulphides. Biotite defines a strong foliation and contains numerous small inclusions of zircon. The feldspars are variably altered. Accessory minerals include (in abundance order) apatite, titanite, pyrite, zircon and ruby.

Swordly inlier*: *intermediate orthogneiss *(RS-SI-18-13; NC 7354 6355)*

In thin section, the sample is dominated by subequal quantities of biotite, quartz and plagioclase and lesser amounts of hornblende and garnet, along with minor skeletal Fe–Ti oxides and more massive sulphides. Biotite defines a weak foliation and occurs as irregular bands, or is disseminated within, a groundmass dominated by anhedral quartz and plagioclase with serrated grain boundaries. Green to brown-green hornblende forms irregularly-shaped, ragged crystals up to 2 mm across. Garnet forms subhedral grains that are up to 1.5 mm in diameter. Most contain sparse inclusions, although some larger grains contain a higher proportion of inclusions. Smaller garnet grains occur within large hornblende crystals, but larger grains show no clear spatial relationship with hornblende. Plagioclase is weakly sericitised. Accessory minerals include (in abundance order) apatite, zircon, rutile and garnet.

2. Sample preparation and grain imaging

All samples were disaggregated by jaw crushing or electric pulse disaggregation using SELFRAG to liberate constituent minerals. Heavy mineral fractions were separated using heavy liquid and magnetic susceptibility techniques. All grains were mounted in 25 mm diameter epoxy stubs and polished to half-grain thickness to expose their interiors. Mounted grains were imaged with transmitted and reflected light on an optical microscope and, subsequently, with a Tescan TIMA, automated quantitative petrological analyser. The TIMA system is based around a scanning electron microscope with an array of EDX detectors, which was used to identify zircon and characterize the sample prior to isotopic analysis, and to produce both phase maps and backscatter electron images. Cathodoluminescence (CL) imaging of zircon grains was undertaken with a Tescan Mira3 variable pressure field emission gun scanning electron microscope (VP-FEG-SEM) at the John de Laeter Centre (JdLC) at Curtin University. Transmitted and reflected light images were used to assess grain shape and transparency as a means to assess zircon growth and modification processes. BSE and CL images were used to document internal zonation patterns (e.g. oscillatory, sector) and identify growth and recrystallization textures as an aid to targeting in situ analysis. CL images of representative analysed grains together with locations of analytical (laser) spots are included as Supplementary Figure 1.

3. Split stream zircon U–Pb and Lu–Hf measurement

Zircon U–Pb and Lu–Hf isotopic measurements were collected simultaneously using the laser ablation split stream system housed in the GeoHistory Facility, JdLC, Curtin University. An overview of operating conditions is given here but more detail is provided in Gardiner et al. (2019). An excimer laser (RESOlution LR 193 nm ArF) was used with a laser fluence of 3 J cm^{-2} and repetition rate of 10 Hz for ~30 to 35 s of total analysis time and 60 s of background capture. All analyses were preceded by three cleaning pulses. The sample cell was flushed by ultrahigh purity He (0.68 L min^{-1}) and N_2 (2.8 mL min^{-1}). Analytical spot diameters were 50 µm. U–Pb data were collected on an Agilent 8900 triple quadrupole mass spectrometer with high purity Ar as the carrier gas (flow rate 0.98 L min^{-1}). Analyses of unknowns were bracketed with analyses of the primary zircon reference material 91500 (1062.4 ± 0.4 Ma; Wiedenbeck et al., 1995) to monitor and correct for mass fractionation and instrumental drift. A range of secondary zircon reference materials spanning Archean to Phanerozoic ages R33 (419.26 ± 0.39 Ma; Black et al., 2004), GJ1 (601.86 ± 0.37 Ma; Horstwood et al., 2016; Jackson et al., 2004), and OG1 (3465.4 ± 0.6 Ma; Stern et al., 2009) were used to monitor data accuracy and precision, and were corrected for mass bias and fractionation based on measured isotopic ratios of the primary reference material. During the analytical sessions, R33, GJ1 and OG1 yielded weighted mean ages of 419 ± 3 Ma ($^{238}U/^{206}Pb$; MSWD = 2, n = 15), 605 ± 3 Ma ($^{238}U/^{206}Pb$; MSWD = 2.2, n = 15), and 3471 ± 7 ($^{207}Pb/^{206}Pb$; MSWD = 1, n =11), respectively, all of which are within 2σ of the published age.

Lu–Hf isotopic data were collected from the same analytical volume as U–Pb data on a Nu Instruments Plasma II MC-ICPMS. Measurements of ^{172}Yb, ^{173}Yb, ^{175}Lu, ^{176}Hf + Yb + Lu, ^{177}Hf, ^{178}Hf, ^{179}Hf and ^{180}Hf were made simultaneously. Mud Tank zircon was used as the primary reference material for Hf isotope ratios, with a ^{176}Hf/^{177}Hf ratio of 0.282505 ± 0.000044 (Woodhead and Hergt, 2005). 91500 (0.282306 ± 0.000008; Woodhead and Hergt, 2005), FC1 (0.282172 ± 0.000042; Salters and Hart, 1991) and GJ-1 (0.282000 ± 0.000005; Morel et al., 2008) were used as secondary standards to monitor accuracy of data processing. During the analytical sessions, secondary standards yielded ^{176}Hf/^{177}Hf weighted average ratios: 91500 = 0.2823128 ± 0.0000089 (MSWD = 1, n = 13); FC1 = 0.282190 ± 0.000011 (MSWD = 0.41, n = 5), and; GJ-1 = 0.2820158 ± 0.000009 (MSWD = 1.4, n = 12). The stable ^{180}Hf/^{177}Hf ratio for Mud Tank was 1.88687 ± 0.000035 overlapping with the expected terrestrial value.

For Loch Fada Inlier sample RS-MTZ-18-01 only, U–Pb and Lu–Hf isotopic data were acquired in separate laser ablation runs rather than by split streaming. Four the four inlier samples dated by Friend et al. (2008), Lu–Hf isotopic data were acquired using the analytical conditions detailed above. For these samples, analytical sites for Lu–Hf did not coincide with those for U–Pb data acquisition, and $\varepsilon Hf_{(t)}$ values are calculated for the interpreted magmatic age of the sample rather than for the measured age of individual spots.

4. Results

Results are compiled in Supplementary Tables 1 and 2. U–Pb data are plotted on Tera-Wasserburg Concordia diagrams in Figure 3 of the main paper. Calculated mean ages discussed below are based on combined ^{207}Pb/^{206}Pb ratios of analyses less than 10% discordant (based on comparison of ^{207}Pb/^{206}Pb and ^{206}Pb/^{238}U ages) and are quoted at ± 2σ uncertainty. $\varepsilon Hf_{(t)}$ values for the least discordant analyses, as plotted on Fig 4 of the main paper, were calculated using ^{176}Lu decay constant 1.865 x $10^{-11}y^{-1}$ (Scherer et al. 2001). Typical 2σ uncertainty on $\varepsilon Hf_{(t)}$ values is ± 0.9 ε units per spot. Model ages were calculated using CHUR and DM parameters as adopted by Blichert-Toft and Albarède (1997) and Griffin et al. (2000). Two-stage model ages $T_{DM(2)}$ assume stage 1 ^{176}Lu/^{177}Hf of 0.015.

Loch Fada inlier: intermediate orthogneiss *RS-MTZ-18-01*

The zircons separated from this mylonite were light brown, mostly subhedral grains, typically 100 to 150 μm in length. CL imaging reveals magmatic internal zonation, with some grains nucleated on older cores with truncated growth zones. Sixty U–Pb analyses were performed on 60 zircon grains. Most analyses are less than 10% discordant. Three analyses (Group D) are greater than 10% discordant and may have undergone variable degrees of radiogenic-Pb loss. The remaining 57 analyses cluster into three age groups (Fig 3). Three core analyses yield a mean $^{207}Pb/^{206}Pb$ age of ca. 2935 Ma, interpreted as the age of an inherited component. Twenty-eight analyses (Group I) yield a weighted mean $^{207}Pb/^{206}Pb$ age of 2823 ± 14 Ma (MSWD = 0.17), interpreted as the age of a magmatic component incorporated into this sample. Twenty-six analyses (Group Z) yield a weighted mean $^{207}Pb/^{206}Pb$ age of 2766 ± 14 Ma (MSWD = 0.72), interpreted as the age of a second magmatic component. Twenty-one of the dated grains were selected for Lu–Hf analysis. The Hf isotopic compositions of both identified magmatic age groups are similar, with $\varepsilon Hf_{(t)}$ values ranging from –2.1 to +0.1 (Fig 4), corresponding to $T_{DM(2)}$ model ages of 3.41 to 3.30 Ga.

Achininver inlier: felsic orthogneiss *RS-TI-18-05*

Twenty analyses were performed on 20 zircon grains. CL imaging reveals well-developed primary magmatic zoning. Some grains contain rounded cores exhibiting oscillatory or contorted zonation. The data cluster into two groups on Concordia and scatter away from the younger of these groups into discordant space (Fig 3). Five analyses (Group D) are greater than 10% discordant and appear to have undergone variable degrees of radiogenic Pb loss. An additional five analyses (Group P) less than 10% discordant have variable $^{207}Pb/^{206}Pb$ ages of 2678–2600 Ma, but may have also lost radiogenic Pb or reflect mixtures with domains that have lost Pb. Eight analyses (Group I) yield a weighted mean $^{207}Pb/^{206}Pb$ age of 2736 ± 14 Ma (MSWD = 1.5) interpreted as the magmatic crystallization age. $\varepsilon Hf_{(t)}$ values for this group range from –2.8 to +3.0 (Fig 4), corresponding to $T_{DM(2)}$ model ages of 3.37 to 3.02 Ga. Two analyses (Group X) with $^{207}Pb/^{206}Pb$ ages (1σ) of 2883 ± 11 Ma and 2838 ± 14 Ma are interpreted as xenocrystic components. $\varepsilon Hf_{(t)}$ values for these are +2.8 and –7.0, respectively. The latter has a $T_{DM(2)}$ model age of 3.64 Ga.

Achininver inlier: intermediate orthogneiss *RS-TI-18-10*

Only a very small zircon fraction was recovered from this sample. Six analyses were performed on six zircon grains (Fig 3), most of which exhibit normal discordance. Three analyses (Group D) are greater than 10% discordant and may have undergone variable degrees of radiogenic-Pb loss. A further three analyses (Group P) are less than 10%

discordant but have variable $^{207}Pb/^{206}Pb$ ages of 2714–2576 Ma. These three analyses may have lost radiogenic Pb relatively early or reflect mixtures of domains of different age that have lost Pb. The most concordant analysis in this group, with a $^{207}Pb/^{206}Pb$ age (1σ) of 2687 ± 14 Ma, gives our best estimate of the minimum crystallization age for the precursor igneous rock. $\varepsilon Hf_{(t)}$ for this spot is –0.2 ($T_{DM(2)}$ 3.21 Ga). The discordant points form a trend of increasingly negative $\varepsilon Hf_{(t)}$ values with lowering $^{207}Pb/^{206}Pb$ age (Fig 4).

Felsic clast in Moine basal conglomerate *RS-TI-18-07*

Twenty analyses were performed on 20 zircon grains. The zircon grains reveal both oscillatory and homogeneous textures under CL; no clear overgrowths are visible. The data cluster into one dominant group on Concordia with additional scatter of analyses into discordant space, showing evidence of older ages with greater radiogenic Pb loss (Fig 3). Three analyses (Group D) are greater than 10% discordant and appear to have undergone variable degrees of radiogenic Pb loss. Three further analyses (Group P) less than 10% discordant have variable $^{207}Pb/^{206}Pb$ ages of 2666–2657 Ma, but may have also lost radiogenic Pb or reflect mixtures with domains that have lost Pb. Thirteen analyses yield a weighted mean $^{207}Pb/^{206}Pb$ age of 2701 ± 16 Ma (MSWD = 2.5), interpreted as the magmatic crystallization age. $\varepsilon Hf_{(t)}$ values for this group range from –0.7 to +1.7 (Fig 4), corresponding to $T_{DM(2)}$ model ages of 3.22 to 2.93 Ga. One analysis, with an error ellipse that is 6.4% discordant at two sigma limits, yields a $^{207}Pb/^{206}Pb$ age (1σ) of 2851 ± 10 Ma that we interpret as a minimum age of a xenocrystic component. $\varepsilon Hf_{(t)}$ for this spot is +0.3 ($T_{DM(2)}$ 3.28 Ga).

Felsic clast in Moine basal conglomerate *RS-TI-18-09*

Thirty analyses were performed on 30 zircon grains. Zircons isolated from this sample are dominantly rounded, colourless to light brown, and stubby. CL images reveal grains with variable emission, but which generally display idiomorphic zoning. All have rounded terminations and some have spherical grain shapes. The data spread along Concordia with all analyses within 10% discordance thresholds (Fig 3). Ten analyses (Group I) of oscillatory zoned zircon yield a weighted mean $^{207}Pb/^{206}Pb$ age of 2725 ± 14 Ma (MSWD = 2.5), interpreted as the magmatic crystallization age. With one exception, $\varepsilon Hf_{(t)}$ values for this group range from –3.8 to +0.7 (Fig 4), corresponding to $T_{DM(2)}$ model ages of 3.43 to 3.16 Ga. The exception has $\varepsilon Hf_{(t)}$ –6.5 ($T_{DM(2)}$ 3.63 Ga) suggesting an older provenance. Two core analyses (Group X) yield a weighted mean $^{207}Pb/^{206}Pb$ age of 3541 ± 15 Ma (MSWD = 0.0064), interpreted as the age of a xenocrystic component. The mean $\varepsilon Hf_{(t)}$ value for these two is –2.9 (Fig 4), corresponding to a mean $T_{DM(2)}$ model age of c. 4.01 Ga. Eighteen analyses (Group P) with $^{207}Pb/^{206}Pb$ ages between 3398 and 2658 Ma, are either sited on zircon with mottled zoning or are mixtures between different textural components. These analyses are interpreted to reflect mixed analyses or the effects of radiogenic Pb loss. Their Hf compositions form a Pb loss trend beginning at Group X, with increasingly negative $\varepsilon Hf_{(t)}$ with lower $^{207}Pb/^{206}Pb$ age (Fig 4).

***Loch Shin inlier: mafic orthogneiss** RS-LSI-18-21*

CL images reveal zircon grains with variable emission and texture, including oscillatory-zoned grains and homogeneous crystals. Some grains have brightly luminescent overgrowths, but these have widths that are below the spatial resolution of the laser. Twenty-three analyses were performed on 23 zircon grains. The data scatter along Concordia and also trend into discordant space (Fig 3). Six analyses (Group D) are greater than 10% discordant and may have undergone variable degrees of radiogenic Pb loss. Thirteen analyses (Group I) cluster on Concordia and yield a weighted mean $^{207}Pb/^{206}Pb$ age of 1772 ± 39 Ma (MSWD = 1.3), interpreted as the age of magmatic crystallization. With one exception, $\varepsilon Hf_{(t)}$ values for this group range from –17.5 to –11.8 (Fig 4), corresponding to $T_{DM(2)}$ model ages of 3.51 to 3.26 Ga. The exception has $\varepsilon Hf_{(t)}$ –3.5 ($T_{DM(2)}$ 2.64 Ga). Two analyses (Group X) yield a weighted mean $^{207}Pb/^{206}Pb$ age of 2545 ± 36 Ma (MSWD = 0.01), interpreted as the age of an inherited component. The mean $\varepsilon Hf_{(t)}$ value for these two is –4.4 (Fig 4), corresponding to a mean $T_{DM(2)}$ model age of c. 3.35 Ga. Two analyses scatter between Groups X and I with $^{207}Pb/^{206}Pb$ ages of 2451–2345 Ma. They are interpreted to have either lost radiogenic-Pb or reflect a physical mixture between different age components.

***Loch Shin inlier: felsic sheet** RS-LSI-18-20*

CL images reveal zircon grains with variable emission, but also generally display idiomorphic zoning. Fading of zoning, and the lobate margins between domains within the same crystal, may indicate magmatic resorption. Many grains have a low-CL response overgrowths and a very thin mantle of high CL response is ubiquitous. Twenty-three analyses were performed on 23 zircon grains. The data show a tendency towards normal discordance from one discrete age group (Fig 3). Four analyses (Group D) are greater than 10%

discordant and may have undergone variable degrees of radiogenic Pb loss. Nineteen analyses (Group I) cluster on Concordia and yield a weighted mean $^{207}Pb/^{206}Pb$ age of 1711 ± 19 Ma (MSWD = 0.74), interpreted as the age of magmatic crystallization. $\varepsilon Hf_{(t)}$ values for this group range from –1.0 to +4.3 (Fig 4), corresponding to $T_{DM(2)}$ model ages of 2.40 to 2.17 Ga.

***Loch Shin inlier: biotite schist** RS-LSI-18-19*

Only a small zircon fraction was recovered from this sample. In CL images, the grains display a variety of internal textures including concentric growth zoning, homogeneous domains and transgressive resorption fronts. Most grains have very thin rims with low CL response. Ten analyses were performed on 10 zircon grains. The data show a tendency towards normal discordance from two discrete age groups (Fig 3). Four analyses (Group D) are greater than 10% discordant and may have undergone variable degrees of radiogenic Pb loss. Three analyses (Group Y) cluster on Concordia at a weighted mean $^{207}Pb/^{206}Pb$ age of 1802 ± 51 Ma (MSWD = 0.89). $\varepsilon Hf_{(t)}$ values for this group range from –2.1 to +5.9 (Fig 4), corresponding to $T_{DM(2)}$ model ages of 2.62 to 2.15 Ga. A regression line fitted through seven analyses (Groups Y and DY) defines an upper intercept of 1846 ± 56 Ma, consistent with the above mean age, with an imprecise Neoproterozoic lower intercept (MSWD = 1.9). The upper intercept age is interpreted as the best estimate of the magmatic crystallization age of a detrital component incorporated into this rock, and hence a maximum age for deposition. A separate regression line through three analyses (Groups S and DS) with older $^{207}Pb/^{206}Pb$ ages, intercepts Concordia at 2485 ± 88 Ma, interpreted as the age of an older detrital component in the schist, with an imprecise recent lower intercept (MSWD = 0.024). $\varepsilon Hf_{(t)}$ values for this group range from –6.4 to –4.1 (Fig 4), corresponding to $T_{DM(2)}$ model ages of 3.40 to 3.18 Ga.

***Swordly inlier: intermediate orthogneiss** RS-SI-18-13*

In CL images, some zircon grains display concentric growth zoning which is truncated at grain edges. All grains have rims of high CL response and some have distinct high CL response cores. Most grains are rounded due to overgrowths. Nineteen analyses were performed on 19 zircon grains. The data spread along Concordia (Fig 3). Thirteen analyses are outside the 10% discordance limit. The remaining six analyses (Group P) yield $^{207}Pb/^{206}Pb$ ages that range from 1655 to 960 Ma, with a significant age component at 1008 ±

68 Ma (MSWD = 0.55) defined by three grains. A correlation between higher U content and younger $^{207}Pb/^{206}Pb$ ages is consistent with the range of concordant dates reflecting radiogenic Pb loss from a c. 1655 Ma component during a c. 1008 Ma metamorphic overprint, or the physical mixture during ablation of these two age components. $\varepsilon Hf_{(t)}$ values for Group P range from –3.9 to +3.5, with those analyses with youngest $^{207}Pb/^{206}Pb$ ages having the most negative $\varepsilon Hf_{(t)}$ values (Fig 4), again consistent with a Pb loss trend. $T_{DM(2)}$ model ages for this group range from 2.15 to 1.79 Ga.

Ribigill, Borgie, Farr and Glenelg–Attadale Inliers

The results of Hf isotope analyses of these previously dated samples (Friend et al. 2008) are included in Supplementary Table 2. $\varepsilon Hf_{(t)}$ values are calculated for the interpreted mean magmatic age of each inlier sample, namely c. 2760 Ma (sample S99/2 Ribigill); c. 2905 Ma (sample S99/1 Farr); c. 2880 Ma (sample S96-12 Borgie); c. 2677 Ma (sample S96-41 Glenelg–Attadale, Western Unit). Similar ranges in $\varepsilon Hf_{(t)}$ were measured for each. For S99/2 Ribigill, $\varepsilon Hf_{(t)}$ ranges from –0.4 to +0.8 (Fig 4), corresponding to $T_{DM(2)}$ model ages of 3.25 to 3.17 Ga. For S99/1 Farr, $\varepsilon Hf_{(t)}$ ranges from –1.6 to +2.1, corresponding to $T_{DM(2)}$ of 3.44 to 3.20 Ga. For S96/12 Borgie, $\varepsilon Hf_{(t)}$ ranges from +1.1 to +2.8, corresponding to $T_{DM(2)}$ of 3.25 to 3.14 Ga. For S96/41 Glenelg–Attadale, $\varepsilon Hf_{(t)}$ ranges from –2.6 to +2.3, corresponding to $T_{DM(2)}$ of 3.33 to 3.02 Ga.

5. References

Black, L.P., Kamo, S.L., Allen, C.M., Davis, D.W., Aleinikoff, J.N., Valley, J.W., Mundil, R., Campbell, I.H., Korsch, R.J., Williams, I.S., and Foudoulis, C., 2004, Improved $^{206}Pb/^{238}U$ microprobe geochronology by the monitoring of a trace-element-related matrix effect; SHRIMP, ID–TIMS, ELA–ICP–MS and oxygen isotope documentation for a series of zircon standards: Chemical Geology, v. 205, p. 115–140, doi: 10.1016/j.chemgeo.2004.01.003.

Blichert-Toft, J., and Albarède, F., 1997, The Lu-Hf isotope geochemistry of chondrites and the evolution of the mantle-crust system: Earth and Planetary Science Letters, v. 148, p. 243-258, doi: 10.1016/S0012-821X(97)00040-X.

Friend, C.R.L., Strachan, R.A., and Kinny, P.D., 2008, U–Pb zircon dating of basement inliers within the Moine Supergroup, Scottish Caledonides: implications of Archaean protolith ages: Journal of the Geological Society, London, v. 165, p. 807-815, doi: 10.1144/0016-76492007-125.

Gardiner, N. J., Kirkland, C. L., Hollis, J., Szilas, K., Steenfelt, A., Yakymchuk, C., and Heide-Jørgensen, H., 2019, Building Mesoarchaean crust upon Eoarchaean roots: the Akia Terrane, West Greenland: Contributions to Mineralogy and Petrology, v. 174, 20, doi: 10.1007/s00410-019-1554-x.

Griffin, W.L., Pearson, N.J., Belousova, E., Jackson, S.E., O'Reilly, S.Y., van Achterberg, E., and Shee, S.R., 2000, The Hf isotope composition of cratonic mantle: LAM-MC-ICPMS analysis of zircon megacrysts in kimberlites: Geochimica et Cosmochimica Acta, v. 64, p. 133-147, doi: 10.1016/S0016-7037(99)00343-9.

Holdsworth, R.E., Strachan, R.A., and Alsop, G.I., 2001, Geology of the Tongue District: Memoir of the British Geological Survey, HMSO.

Horstwood, M.S.A., Košler, J., Gehrels, G., Jackson, S.E., McLean, N.M., Paton, C., Pearson, N.J., Sircombe, K., Sylvester, P., Vermeesch, P., Bowring, J.F., Condon, D.J., and Schoene, B., 2016, Community-derived standards for LA-ICP-MS U-(Th-)Pb geochronology – uncertainty propagation, age interpretation and data reporting: Geostandards and Geoanalytical Research, v. 40, p. 311–332, doi: 10.111/j.1751-908X.2016.00379.x.

Jackson, S.E., Pearson, N.J., Griffin, W.L., and Belousova, E.A., 2004, The application of laser ablation-inductively coupled plasma-mass spectrometry to in situ U-Pb zircon geochronology: Chemical Geology, v. 211, p. 47–69, doi: 10.1016/j.chemgeo.2004.06.017.

Morel, M.L.A., Nebel, O., Nebel-Jacobsen, Y.J., Miller, J.S., and Vroon, P.Z., 2008, Hafnium isotope characterization of the GJ-1 zircon reference material by solution and laser-ablation MC-ICPMS: Chemical Geology, v. 255, p. 231–235, doi: 10.1016/j.chemgeo.2008.06.040.

Read, H.H., and Phemister, J., 1926, The geology of Strath Oykell and Lower Loch Shin: Memoir of the Geological Survey, Scotland.

Salters, V.J.M., and Hart, S.R., 1991, The mantle sources of ocean ridges, islands and arcs: the Hf-isotope connection: Earth and Planetary Science Letters, v. 104, p. 364–380, doi: 10.1016/0012-821X(91)90216-5.

Scherer, E., Münker, C., and Mezger, K., 2001, Calibration of the Lutetium–Hafnium Clock: Science, v. 293, p. 683-687, doi: 10.1126/science.1061372.

Stern, R.A., Bodorkos, S., Kamo, S.L., Hickman, A.H. and Corfu, F., 2009, Measurement of SIMS instrumental mass fractionation of Pb isotopes during zircon dating: Geostandards and Geoanalytical Research, v. 33, p. 145-168, doi: 10.1111/j.1751-908X.2009.00023.x.

Wiedenbeck, M., AllÉ, P., Corfu, F., Griffin, W.L., Meier, M., Oberli, F., Quadt, A.V., Roddick, J.C., and Spiegel, W., 1995, Three natural zircon standards For U-Th-Pb, Lu-Hf, trace element and REE analyses: Geostandards Newsletter, v. 19, p. 1–23, doi: 10.1111/j.1751-908X.1995.tb00147.x.

Woodhead, J.D., and Hergt, J.M., 2005, A preliminary appraisal of seven natural zircon reference materials for in situ Hf isotope determination: Geostandards and Geoanalytical Research, v. 29, p. 183–195, doi: 10.1111/j.1751-908X.2005.tb00891.x.

Supplementary Figure 1

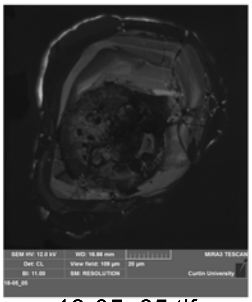
18-05_05.tif

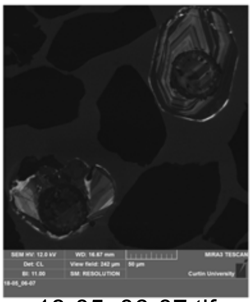
18-05_06-07.tif

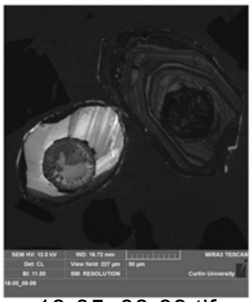
18-05_08-09.tif

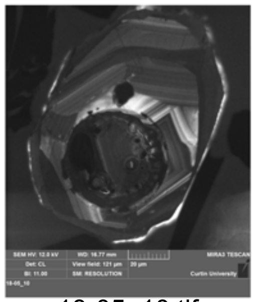
18-05_10.tif

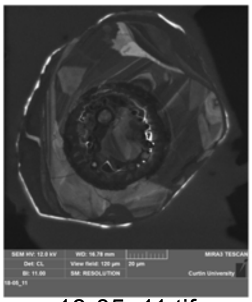
18-05_11.tif

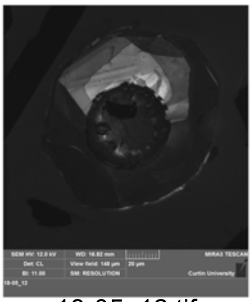
18-05_12.tif

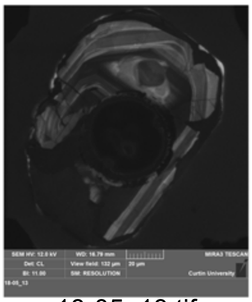
18-05_13.tif

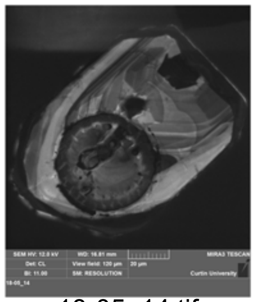
18-05_14.tif

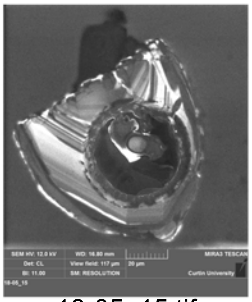
18-05_15.tif

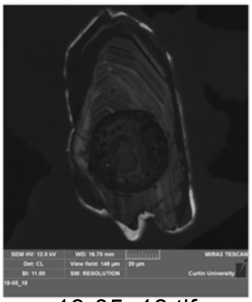
18-05_18.tif

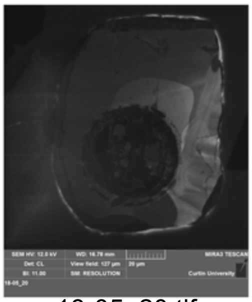
18-05_20.tif

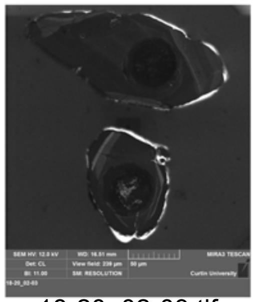
18-20_02-03.tif

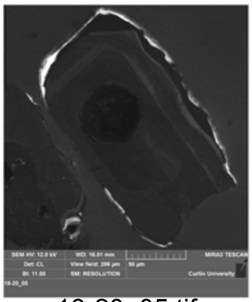
18-20_05.tif

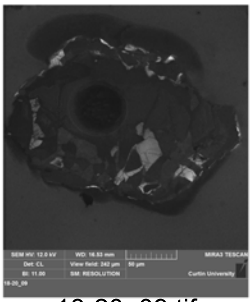
18-20_09.tif

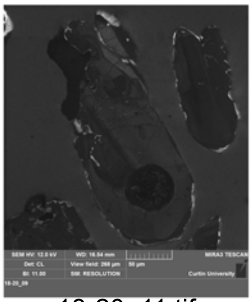
18-20_11.tif

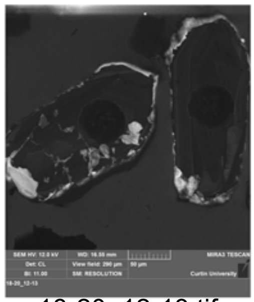
18-20_12-13.tif

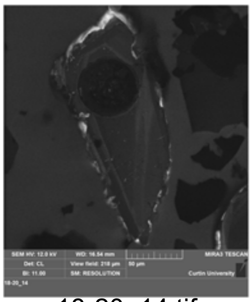
18-20_14.tif

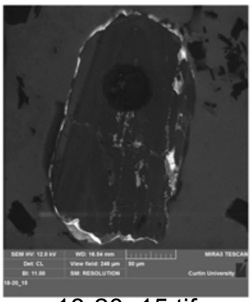
18-20_15.tif

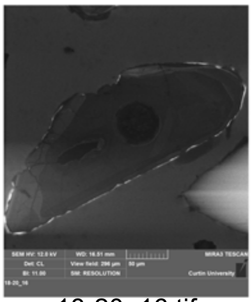
18-20_16.tif

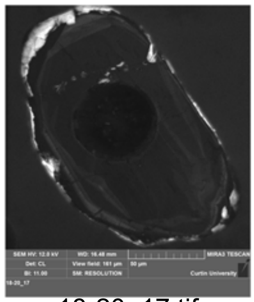
18-20_17.tif

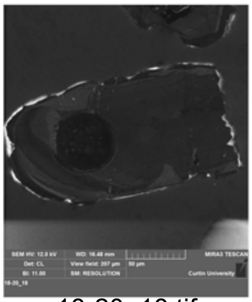
18-20_18.tif

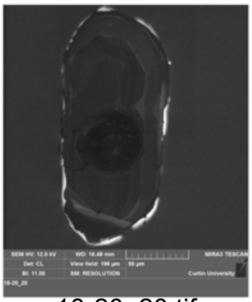
18-20_20.tif

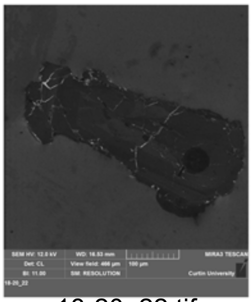
18-20_22.tif

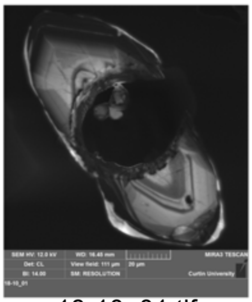
18-10_01.tif
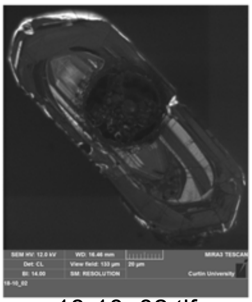
18-10_02.tif
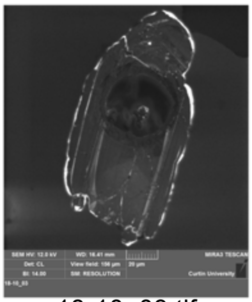
18-10_03.tif
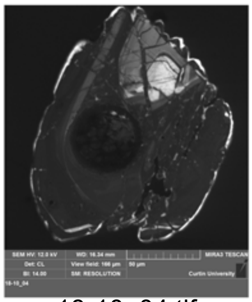
18-10_04.tif
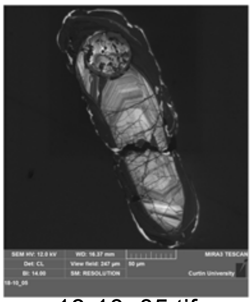
18-10_05.tif
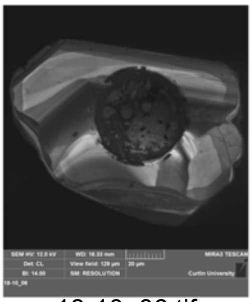
18-10_06.tif
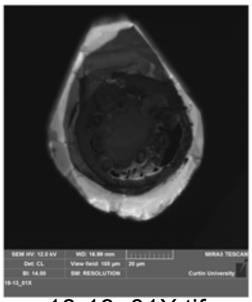
18-13_01X.tif
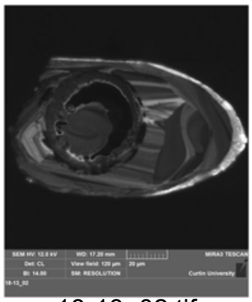
18-13_02.tif
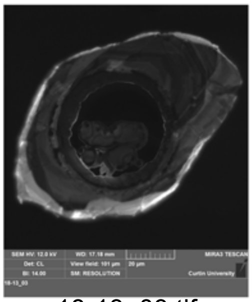
18-13_03.tif
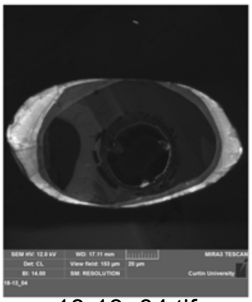
18-13_04.tif
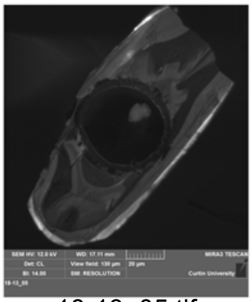
18-13_05.tif
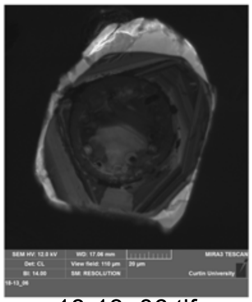
18-13_06.tif

18-13_07.tif
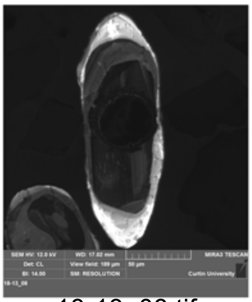
18-13_08.tif
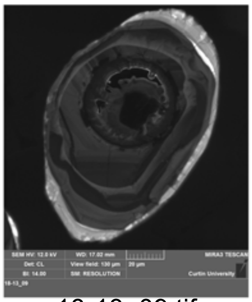
18-13_09.tif
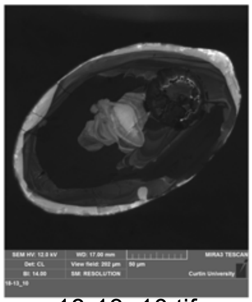
18-13_10.tif
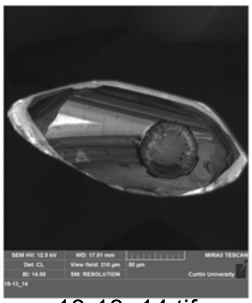
18-13_14.tif
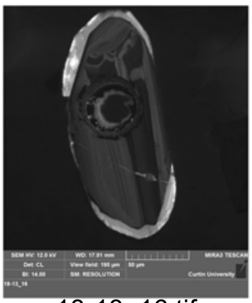
18-13_16.tif

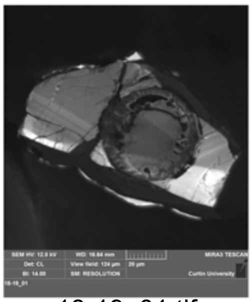
18-19_01.tif

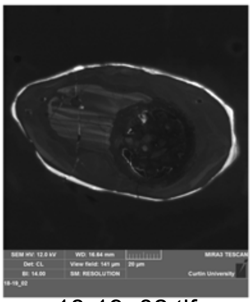
18-19_02.tif

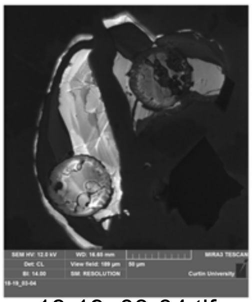
18-19_03-04.tif

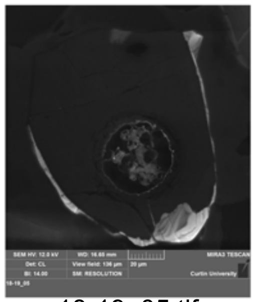
18-19_05.tif

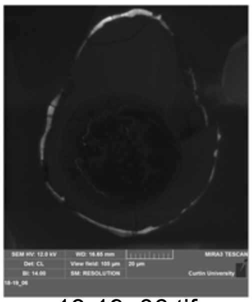
18-19_06.tif

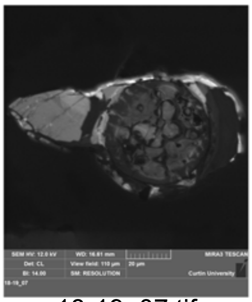
18-19_07.tif

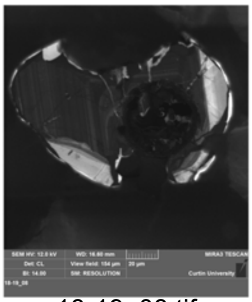
18-19_08.tif

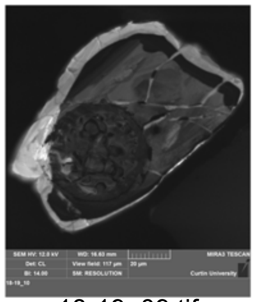
18-19_09.tif

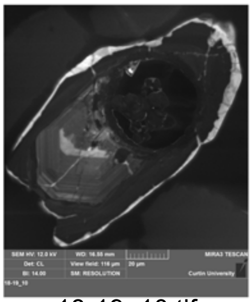
18-19_10.tif

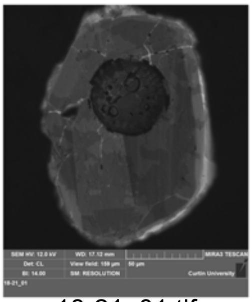
18-21_01.tif

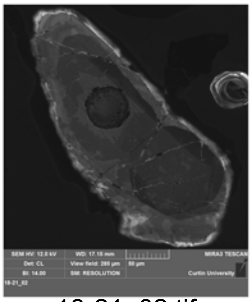
18-21_02.tif

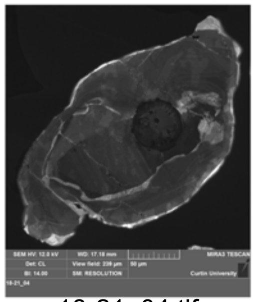
18-21_04.tif

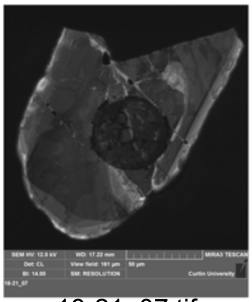
18-21_07.tif

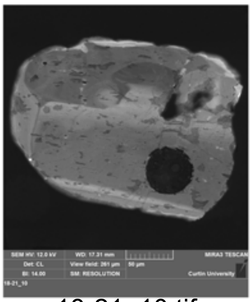
18-21_10.tif

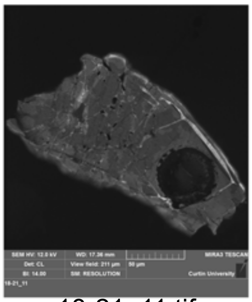
18-21_11.tif

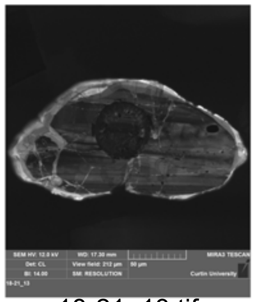
18-21_13.tif

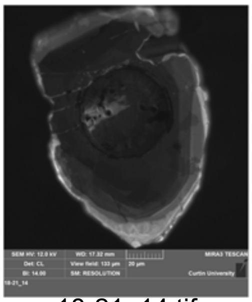
18-21_14.tif

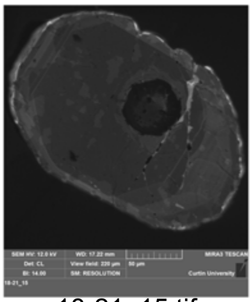
18-21_15.tif

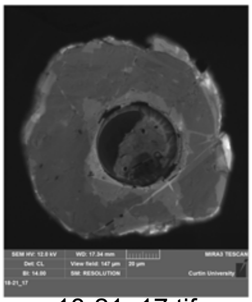
18-21_17.tif

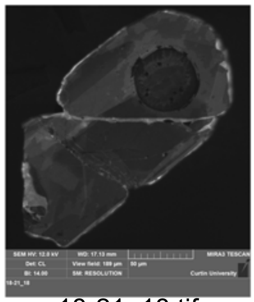
18-21_18.tif

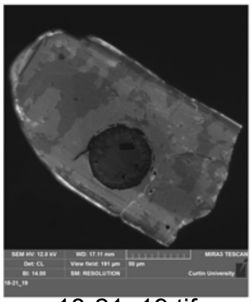
18-21_19.tif

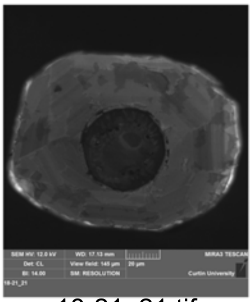
18-21_21.tif

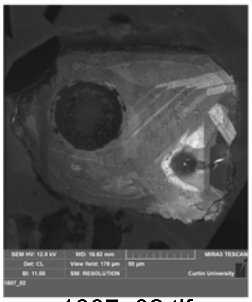
1807_02.tif

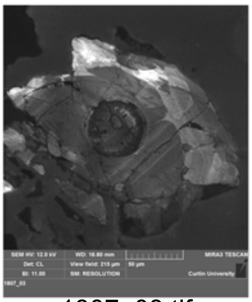
1807_03.tif

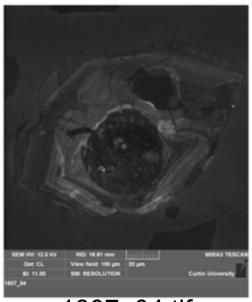
1807_04.tif

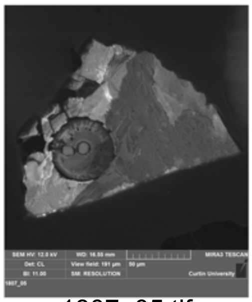
1807_05.tif

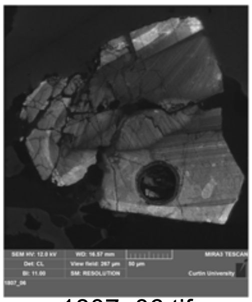
1807_06.tif

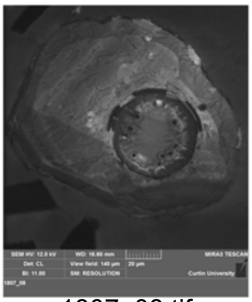
1807_08.tif

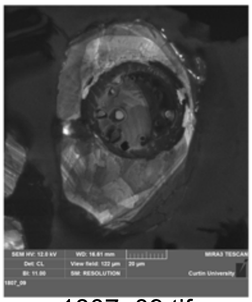
1807_09.tif

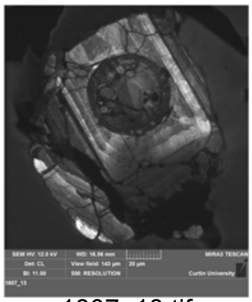
1807_13.tif

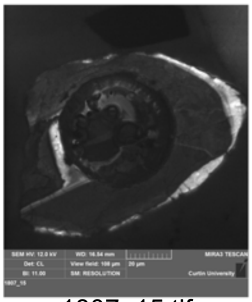
1807_15.tif

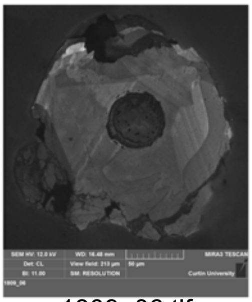
1809_06.tif

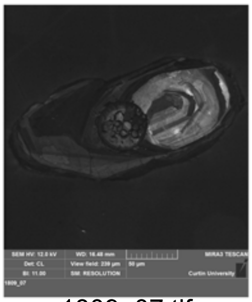
1809_07.tif

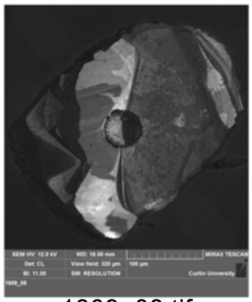
1809_08.tif

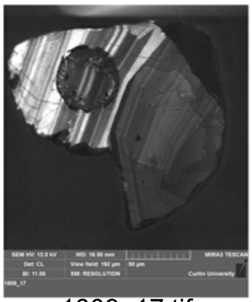
1809_17.tif

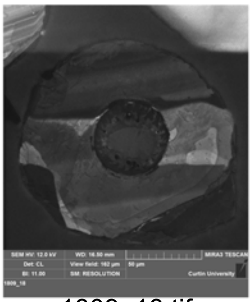
1809_18.tif

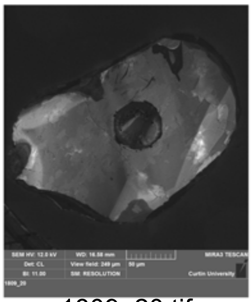
1809_20.tif

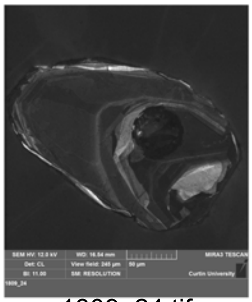
1809_24.tif

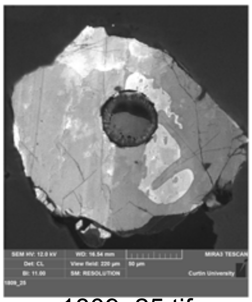
1809_25.tif

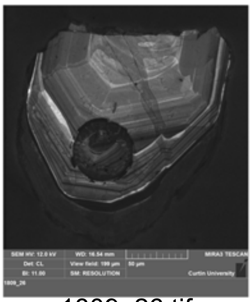
1809_26.tif

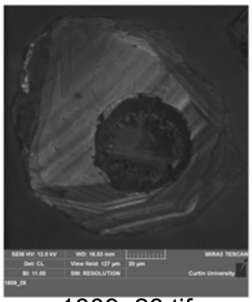
1809_28.tif